
ARTICLE

Investigation of high energy particle dynamics in a linear inertial electrostatic confinement fusion device by particle-in-cell Monte Carlo collision method

Kazuhiro Matsuda and Jun Hasegawa *

*Laboratory for Zero-Carbon Energy, Institute of Integrated Research, Institute of Science Tokyo,
2-12-1 Ookayama, Meguro-ku, Tokyo 152-8550, Japan*

Particle dynamics inside an inertial electrostatic confinement (IEC) fusion neutron source was analyzed using a one-dimensional Particle-In-Cell Monte-Carlo-collision (PIC-MCC) simulation code, which considers five kinds of ion/neutral particle species (H_2^+ , H^+ , H_3^+ , H_2 , H) as well as electrons. The relationship between discharge sustaining voltage and background gas pressure (Paschen curve) was compared between the simulation and the experiment to check the reliability of the simulation code. A Balmer- α emission spectrum from hydrogen plasma was also predicted from the calculated phase distribution of hydrogen atoms, which well explained the spectrum observed by spectroscopic measurement. The simulation results showed that most of the input power was converted to electron kinetic energies and eventually consumed as heat load to the anode.

Keywords: *neutron source; inertial electrostatic confinement fusion; glow discharge; particle-in-cell simulation; Monte-Carlo collision method*

1. Introduction

Since the recent development and construction of accelerator-driven neutron sources such as J-PARC [1] and RIKEN RANS [2], the use of neutrons in various fields has progressed. However, the number of these facilities is still limited due to their high construction cost, preventing the use of neutrons in relatively small industrial and academic research facilities. Fission neutron sources such as ^{252}Cf are used in many facilities, but they have the disadvantage of relatively low intensity in addition to high management cost as radioactive materials. Inertial electrostatic confinement (IEC) fusion neutron sources are much smaller and less expensive than accelerator-driven neutron sources. In addition, because of their relatively high portability, IECs are expected to be compact neutron sources that can be used not only in research facilities but also in the field outdoors. Another important feature of the IEC fusion neutron source is that, unlike fission neutron sources, neutron production can be stopped by turning off the power.

One of the most important issues of the IEC fusion neutron source is improving the neutron production rates (NPR). NPRs of $\sim 10^8$ n/s have been achieved in previously developed IEC D-D fusion neutron sources [3-6]. To achieve NPRs more than 10^9 n/s, it is inevitable to increase the electric input power, which probably brings serious problems to the discharge electrodes due to excessive heat

load originating from high-energy particle bombardment. Therefore, it is very important to understand the behavior of energetic particles in the IEC device and feedback that knowledge to the device design. Our research group has developed a linear-type IEC device [7] and been studying particle behavior in the device by combining Doppler spectroscopy and numerical analyses based on Monte-Carlo particle tracking [8]. In those analyses we assumed vacuum potential between electrodes because the degree of ionization of background gas in the IEC device was typically quite low. However, if the input power is increased, the potential modulation due to the ion space charge effect becomes remarkable.

In this study, numerical analyses including space-charge effects is performed by an originally developed one-dimensional simulation code based on the Particle-In-Cell Monte-Carlo-Collision (PIC-MCC) method. We examine the dynamics of plasma particles in the linear-type IEC device and clarify the energy distributions of energetic particles that bombard the electrodes and deposit heat to them. To check the reliability of the developed code, we also perform the spectroscopic measurement for hydrogen plasma generated in the IEC device and compare the result with the simulated one.

2. Methods

2.1. Experimental

Figure 1(a) shows a cross-sectional view of the linear-type IEC fusion device that we developed as a compact neutron source. The figure also schematically explains the

*Corresponding author. E-mail: jhasegawa@zc.iir.isct.ac.jp

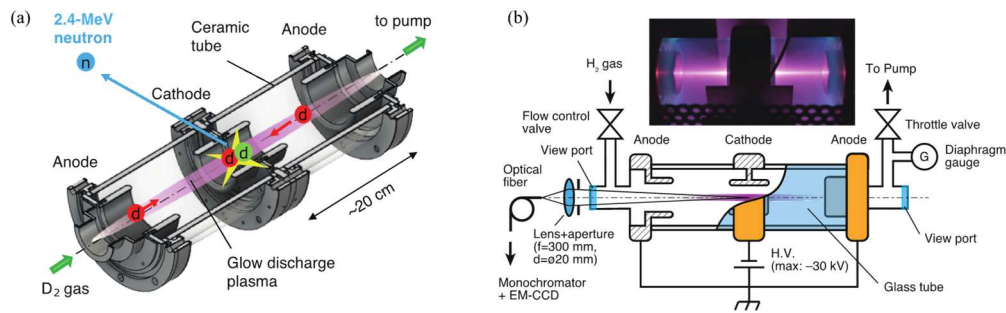


Figure 1. (a) A cross-sectional view of the developed linear-type IEC device, (b) an experimental setup for Doppler spectroscopy.

principle of neutron generation. The overall structure of the device is axisymmetric. A hollow cathode and two facing anodes made of stainless steel are arranged coaxially on the center axis with gap lengths of 115 mm. The electrical insulation between the electrodes is established by 8-mm-thick alumina ceramic tubes with an inner diameter of 134 mm. The cathode has an inner diameter of 60 mm and a length of 100 mm. The anode has an inner diameter of 75 mm. Deuterium gas is supplied from one end of the device and evacuated from the other end. A cathode voltage of typically ~ 100 kV causes glow discharge along the center axis of the device, which produces deuterium ions (“red” particle in Figure 1(a)). These ions are accelerated by electric fields toward the cathode and some of them collide with background deuterium molecules (“green” particle) to cause D-D fusion reactions. The generated 2.45-MeV neutrons are isotropically emitted and taken out of the device for use.

In this study we used an IEC device prepared for “cold” experiments without neutron generation. The device has exactly the same dimensions and structure as the IEC fusion neutron source in Figure 1(a), but uses borosilicate glass as the insulator material. An experimental setup used in this study is shown in Figure 1(b). Instead of deuterium, hydrogen was supplied through a solenoid valve with a flow rate of ~ 1 -2 sccm and evacuated by a turbo molecular pump through a throttle valve. The pumping speed was feed-back controlled by the throttle valve to maintain gas pressure in the glass tube to be a certain value. The cathode was biased to -30 kV by a regulated high-voltage power supply to induce high-voltage glow discharge in hydrogen gas. The power supply was operated in a constant current mode and the discharge voltage was indirectly controlled by changing the hydrogen gas pressure. A typical discharge pattern is also shown in Figure 1(b). A bright plasma column was formed along the center axis of the device.

Spectroscopic measurement of hydrogen Balmer series emission from plasma was also performed using a 50-cm monochromator (grating: 600 cm^{-1}) combined with a high-resolution EMCCD camera (pixel size: $16\text{ }\mu\text{m}\times 16\text{ }\mu\text{m}$). The light emitted from the region inside the hollow cathode was extracted through the anode center hole and focused by a $\phi 30$ -mm plano-convex lens ($f = 300$ mm) onto the inlet of an optical fiber connected to the spectrometer. The lens was located 560 mm apart from the center of the cathode. An aperture of 5 mm in diameter

was placed just in front of the lens so that the depth of field could be larger than the axial plasma size (~ 200 mm). The wavelength resolution of this spectroscopy system is calculated to be ~ 0.045 nm/px if all aberrations of the optics are ignored.

2.2. Numerical analysis

The one-dimensional PIC-MCC code developed in this study considers five kinds of ion/neutral particle species (H_2^+ , H_2 , H^+ , H , and H_3^+) as well as electrons. As for neutral particles such as H_2 and H , only fast particles generated by charge exchange reactions are tracked, meaning that slow particles existing in the background gas are not tracked. Three-dimensional electrostatic field calculations using a commercially available finite element analysis code (COMSOL Multiphysics[®]) showed that the radial component of the electric field near the central axis of the device is much smaller than the axial component, despite the cylindrical shape of the electrodes. In addition, since this simulation deals only with fast particles accelerated directly (or indirectly) by the axial electric field, the deflection of fast particles by the radial electric field can be considered negligible. These facts support the use of the one-dimensional model in this study.

The PIC part of this code adopts an electrostatic model considering one dimension and three velocities (1d3v) for particle motions. The MCC part takes account of collisions listed in Table 1. To calculate their probabilities, it uses the cross-section data compiled by Tabata, et al. [9] and Yoon, et al. [10]. The code can be applied also to the case of deuterium gas discharge, where fusion reactions between deuterium nuclei are additionally considered using cross sections given by the Duane’s 5-parameter expression [11]. Since the D-D fusion cross sections are much smaller than those for the atomic collisions between hydrogen particles, they are artificially enhanced by 10^8 in the code to obtain a sufficient number of fusion reactions within a practical calculation time. As long as the total number of fusion events due to the increased cross section is negligible compared to other collision events, it will not affect the particle dynamics in the simulation. For calculations of atomic collisions between deuterium particles, the same cross section data as for hydrogen are used by considering equivalent velocities.

In the present analysis, the discharge electrodes were assumed to be parallel flat planes arranged in the order of

Table 1. Collisional processes considered in the PIC-MCC simulation.

$e + H_2 \rightarrow$ (elastic)	$H_2 + H_2 \rightarrow$ fast H^+	$H + H_2 \rightarrow H_2^+$
$e + H_2 \rightarrow 2e + H_2^+$	$H_2 + H_2 \rightarrow H\alpha$	$H + H_2 \rightarrow$ fast H^+
$H_2^+ + H_2 \rightarrow e$ (total)	$D_2 + D_2 \rightarrow$ fusion	$H + H_2 \rightarrow H\alpha$
$H_2^+ + H_2 \rightarrow$ slow H_2^+	$H^+ + H_2 \rightarrow e$ (total)	$(D + D_2 \rightarrow$ fusion)
$H_2^+ + H_2 \rightarrow$ fast H^+	$H^+ + H_2 \rightarrow$ fast H^+	$H_3^+ + H_2 \rightarrow$ fast H^+
$H_2^+ + H_2 \rightarrow H_3^+ + H$	$H^+ + H_2 \rightarrow H\alpha$	$H_3^+ + H_2 \rightarrow$ fast H_2^+
$H_2^+ + H_2 \rightarrow H\alpha$	$(D^+ + D_2 \rightarrow$ fusion)	$H_3^+ + H_2 \rightarrow H\alpha$
$(D_2^+ + D_2 \rightarrow$ fusion)		$(D_3^+ + D_2 \rightarrow$ fusion)

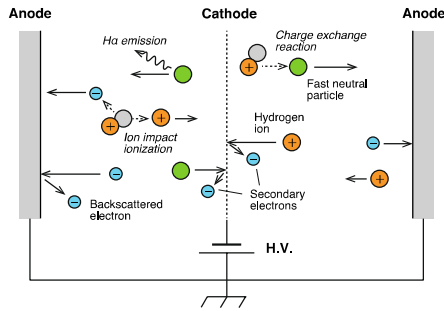


Figure 2. A schematic of the PIC-MCC simulation model.

anode, cathode, and anode as shown in **Figure 2**. The distance between the anode and the cathode was set to 0.2 m. The probability that neutral particles pass through the center translucent cathode was assumed to be constant during the calculation. To reproduce stable discharge in the numerical analysis, the applied voltage was feedback-controlled so that the discharge current flowing between the cathode and the anodes could be a certain constant value. In addition to the collision events in Table 1, both backscattering of electrons that collide the anodes and secondary electron emission from the cathodes due to bombardment of energetic ions and neutral particles were taken into account based on the models given in the literatures [12,13].

To compare with experimental data, the discharge voltages were recorded at various background gas pressures when stable discharge conditions were established in the simulation space. In addition, the positions and velocities of hydrogen atoms decaying in the Balmer- α transition were recorded to reconstruct a $H\alpha$ emission spectrum from plasma. These excited hydrogen atoms are generated not

only by charge exchange collisions between fast H^+ and background H_2 , but also by those between fast H_2^+/H_3^+ and background H_2 with dissociation of excited molecules (H_2^* and H_3^*). In the latter case, we assumed that the generated hydrogen atoms have a half or a third of the kinetic energy that the parent molecular ions gain in the electrostatic field.

3. Results and discussion

The line spectra of $H\alpha$ emission ($\lambda=656.3$ nm) from the IEC device were recorded with various radial positions from 0 to 5 mm as shown in **Figure 3(a)**. These data were taken with a discharge condition of 0.7 Pa, 17.3 kV, and 1 mA. In addition to the center shape peak, large broad Doppler-shift peaks are observed. These Doppler-shift components are due to fast hydrogen atoms generated by charge exchange reactions between hydrogen ions and background molecules. Because the wavelength shift due to the Doppler effect has a one-to-one relationship with the velocity of $H\alpha$ emitting hydrogen atoms, the shape of the Doppler components describes the velocity distribution of those atoms. It is important that although the peak height of the Doppler component decreases with increasing radial distance, its shape remains unchanged. **Figure 3(b)** plots the integrated light intensities of the thermal (center) and the Doppler components versus radial observation position. These intensities have maximum values around the center axis and decreases gradually with radial distance from the center. The shapes of the intensity profiles are very similar in Figure 3(b), indicating that these profiles describe the radial distribution of the plasma density in the IEC device. The results shown in Figure 3 strongly supports the fact that the particle dynamics is almost independent

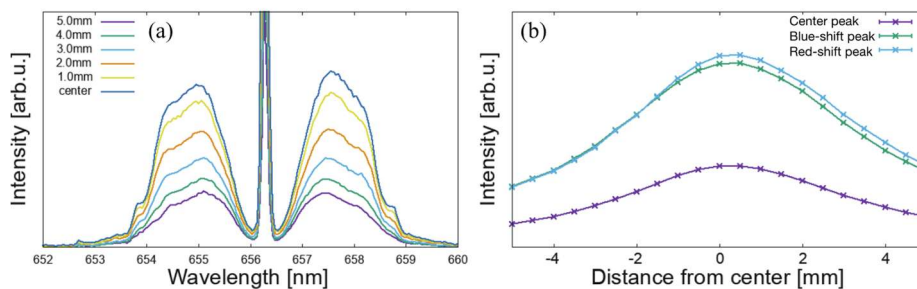


Figure 3. (a) Typical spectra of $H\alpha$ line emission observed in the axial direction and their dependency on radial positions; (b) radial intensity distributions of the Doppler components and the thermal component of $H\alpha$ emission.

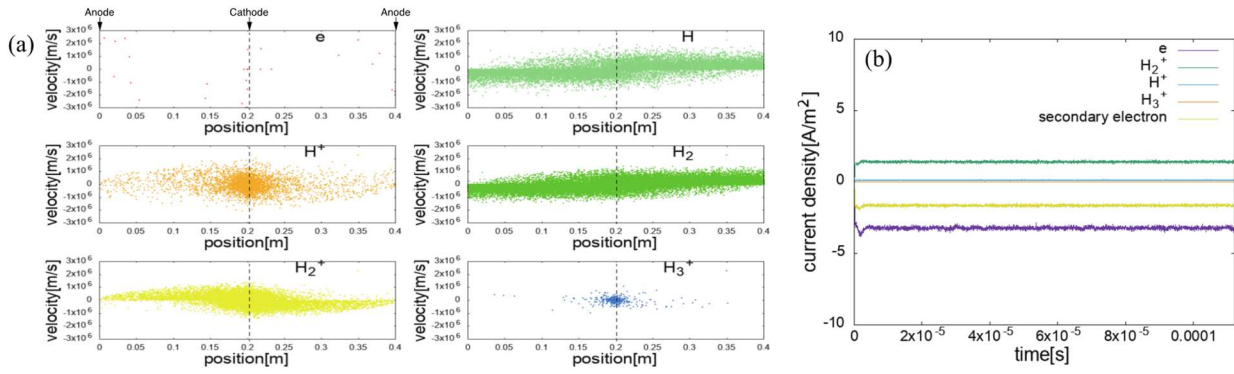


Figure 4. (a) Typical phase space distributions of plasma particles; (b) temporal change of currents delivered by ions and electrons.

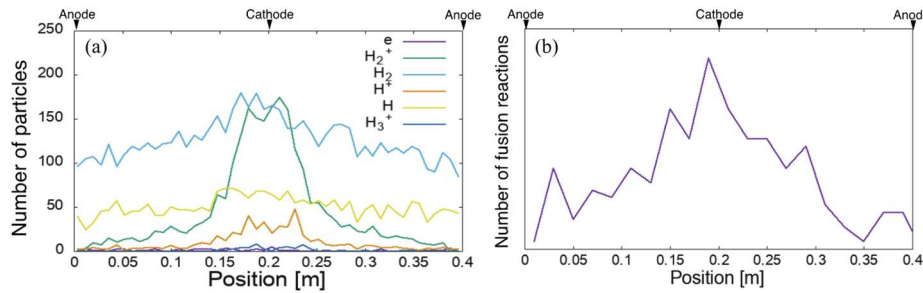


Figure 5. (a) Typical spatial distributions of plasma particles; (b) typical spatial distribution of D-D fusion reactions.

of the radial positions particularly near the center axis. This result is reasonable because the electric field has large axial component near the axis and the acceleration of particles in the radial direction is not so important there as discussed in Section 2.2. Therefore, we consider that our analysis using a one-dimensional PIC-MCC simulation code is useful to discuss the dynamics of the plasma particles in the linear-type IEC device even though the actual electrodes having three-dimensional shapes.

Figure 4(a) shows the typical phase space distributions of plasma particles (e , H , H^+ , H_2 , H_2^+ , and H_3^+) simulated with a discharge condition of 0.7 Pa, 17.6 kV, and 1 mA. Under this condition, most of the electrons generated by ionization processes near the cathode are strongly accelerated by the electric field and then collide with the anodes without any collisions with background hydrogen molecules. The space charge effect due to ions is not strong enough to deform the electrostatic potential significantly, so these electrons are not trapped in the potential and lost within a relatively short time period. Thus, the electron density remains low in Figure 4(a). On the other hand, H^+ and H_2^+ ions are trapped by the electrostatic potential well induced by the externally applied cathode voltage, leading to concentration of ions around the cathode. A lot of energetic neutral particles such as H and H_2 also exist, which are produced by charge exchange reactions between the ions and the background molecules. Their spatial distributions are relatively uniform because of their ballistic motions.

Typical temporal evolutions of currents delivered by plasma ions and electrons to the electrodes are separately shown in **Figure 4(b)**. Since the net current flowing

between the anodes and the cathode is controlled to be constant at 1 mA in this simulation, the initial fluctuations in these currents are quickly suppressed within several microseconds so as to keep a constant discharge condition as in the real experiments. Note that two kinds of electron currents are plotted in this figure. One of them is the incoming electron current measured at the anode (denoted by “ e ”). The other is the outgoing electron current measured at the cathode, which is composed of secondary electrons generated by energetic ion/neutral particle bombardment onto the cathode. As shown in the figure, the difference between these two electron currents is equal to the ion current flowing into the cathode. This is because the net currents flowing from the anode and flowing into the cathode must be balanced (Kirchhoff’s law). The ion current is mainly composed of H_2^+ ions, which are generated not by the electron impact but by the ion impact ionization of H_2 molecules. This result means that the “ β effect” becomes significant in this kind of low-pressure high-voltage discharge, which is characteristic of the IEC devices operated with relatively low-pressure gas (~ 1 Pa).

Spatial distributions of plasma particles calculated with a condition of 0.7 Pa and 17.6 kV are plotted in **Figure 5(a)**. Although some fluctuations are observed in the density distributions, they are not essential and are attributed to insufficient statistics. As shown in the figure, the ions, particularly H_2^+ , have maximum densities around the cathode. As discussed above, this is due to the electrostatic confinement of the ions by the potential well. The density distributions of neutral particles (H and H_2) also exhibit weak dependence on the axial position, originating from the fact that these energetic neutrals are created by charge

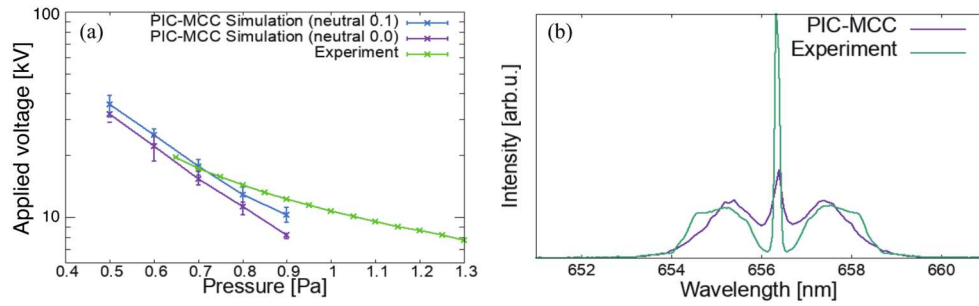


Figure 6. (a) Dependencies of discharge sustaining voltages on background gas pressures; (b) comparison of $H\alpha$ emission spectra between experiment and simulation.

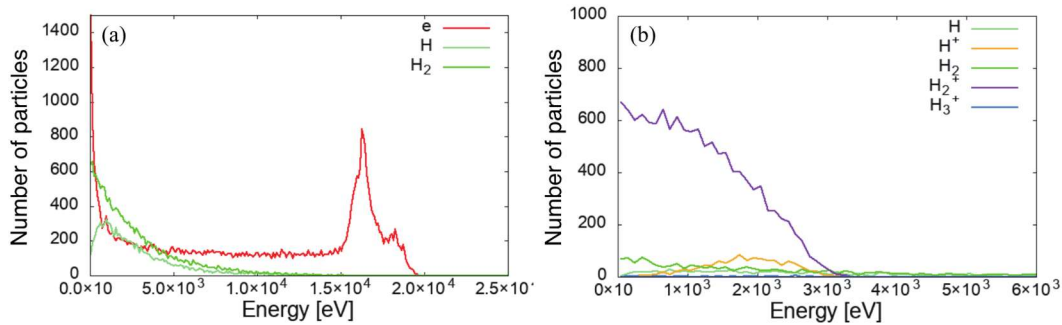


Figure 7. (a) Kinetic energy distributions of anode colliding particles; (b) kinetic energy distributions of cathode colliding particles.

exchange reactions between energetic ions and neutral gas molecules.

Figure 5(b) plots the distribution of D-D fusion reactions obtained with 0.5 Pa and 35.6 kV. Only for this result, we assumed deuterium particles in the simulation. Because the fusion cross section strongly depends on the particle energy, the distribution of the fusion reaction rate has a maximum around the cathode, where the kinetic energy of deuterium ions accelerated by the electrostatic field becomes the highest.

To check the reliability of the simulation, the relationship between background gas pressure and the discharge voltage was investigated and compared with the experiment. Under a fixed discharge current of 1 mA, the discharge sustaining voltages calculated with background pressures from 0.3 to 0.9 Pa are shown in the **Figure 6(a)**. Here, we show two different cases assuming the collision probability of energetic neutral particles with the cathode grid to be 0 or 0.1. The discharge voltage in the simulations tends to decrease with increasing background gas pressure. This tendency well agrees with the experimental result shown in the same figure. In particular, when the collision probability is 0.1, the discharge voltage at 0.7 Pa agrees well between the experiment and the simulation. For simplicity of discussion, all simulation results shown below are for a fixed collision probability of 0.1.

The $H\alpha$ spectra were numerically calculated from the axial velocity distributions of the $H\alpha$ -emitting hydrogen atoms. Because the depth of field of the spectroscopic optics was deep enough to cover the entire length of the plasma column, we accumulated the number of $H\alpha$

emission events in PIC-MCC simulations along the entire computational domain without spatial weighting. One of the examples calculated with a discharge condition of 0.7 Pa, 17.6 kV, and 1 mA is shown in **Figure 6(b)**. The central peak and the left and right Doppler-shift peaks observed by the experiment (**Figure 3(a)**) were reproduced in the simulation. The inflection points on the spectral curve around 653 nm and 659 nm were also reproduced. The quantitative agreement between the numerical analysis and the experiment is not so perfect, but this result supports the reliability of the present analysis to some extent.

Finally, we show the energy distributions of the particles colliding with the anodes (e, H, and H₂) in **Figure 7(a)**. The simulation was performed with a condition of 0.7 Pa, 20 kV, and 1 mA. The electron energy distribution deviates significantly from the Maxwell-Boltzmann distribution because most of the secondary electrons are accelerated from the cathode to the anode without any collision with gas molecules. This is because the cross sections for electron impact ionizations rapidly drop when the electron energy exceeds 1 keV. From the result shown in the figure, about 57% of the anode colliding particles are electrons and their contribution to the heat load is about 82% of the total.

On the other hand, the energy distributions of the particles colliding with the cathode is shown in **Figure 7(b)**. The kinetic energies of most particles are much smaller than the energy equivalent to the applied voltage (20 kV). The particle species that gave the highest heat load to the cathode was H₂⁺, which accounted for about 60% of the

Table 2. Number of plasma particles bombarding electrodes and heat depositions by those particles.

Particle species	Anode		Cathode	
	Number ratio [%]	Heat ratio [%]	Number ratio [%]	Heat ratio [%]
e	46	79.7	0	0
H ₂ ⁺	0.071	0.047	14.9	2.79
H ₂	20.4	8.60	1.92	0.86
H ⁺	0.51	0.25	1.27	0.39
H	13.7	6.69	1.23	0.68
H ₃ ⁺	0	0	0.039	0.01
Total	80.6	95.3	19.4	4.7

total. The heat loads due to the other particles were estimated to be ~19% for H₂, ~8.5% for H⁺, and ~12% for H.

The above simulation results are summarized in **Table 2**. The number of particles impinging on the electrodes and their thermal depositions are shown as ratios relative to the total values. Note that a small fraction of the energetic neutrals (H₂) produced in the charge exchange reaction are ionized again near the anode, so there are H₂⁺ ions that can reach the anode even after deceleration. As shown in the table, ~80% of input power is eventually consumed as heat deposited by electrons on the anodes. This result indicates that for the stable operation of the linear-type IEC neutron source, it is effective to reduce the local concentration of heat delivered by energetic electrons to the anode. If we assume the operation with 100 kV and 30 mA, the simulation predicts that a heat power more than 1 kW is deposited on each anode, leading to the local temperature rise of the anode surface and the emission of impurity gas. Actually, the anode surfaces made of stainless steel were locally damaged (~ø5 mm) in the previous experiments with a long operation time of ~100 h [7]. By diverging the trajectory of the electron beam using a cusp magnetic field near the anode, or by actively cooling the anode using a high melting point material such as tungsten, which has high sputtering resistance, we consider that this issue can be resolved. On the other hand, thermal deposition due to hydrogen/deuterium particles on the cathode is only ~5%. Although this value is not negligible, the cathode temperature rise due to this effect will be easily suppressed thanks to the cathode geometry of the linear-type IEC device, which is suitable for contact heat removal by the coolant.

In this paper, we reported simulation results under relatively low input power operation, where the ion space charge effect is less dominant and limited to only weak modulation of the potential profile between the cathode and anode. On the other hand, at high input power operation for neutron generation (typically ~100 kV and ~30 mA), the ion space charge effect dominates, creating a flat potential region near the anode where many electrons are trapped. The PIC-MCC code is currently being improved to simulate such strong space charge effects.

4. Conclusion

In this study, we analyzed particle kinetics in hydrogen

glow discharge in the linear-type IEC device operated with background gas pressures from 0.3 Pa to 1.0 Pa by using an originally developed 1D PIC-MCC code. The dependence of the discharge sustaining voltage on the background gas pressure, which was predicted by the simulation, showed a good agreement with the experiment. The numerically predicted H α spectrum including the Doppler shift components qualitatively reproduced the experimentally observed one. We found that the heat load on the anodes is mainly provided by energetic electrons and the influence of high-energy atoms and molecules is relatively small. On the other hand, the heat load on the cathode was found to be due mainly to H₂⁺ ions.

References

- [1] Takada, Haga, Teshigawara, Aso, Meigo, Kogawa, Naoe, Wakui, Ooi, Harada and Futakawa, Materials and Life Science Experimental Facility at the Japan Proton Accelerator Research Complex I: Pulsed Spallation Neutron Source, *Quantum Beam Science* 1.8 (2018), <https://doi.org/10.3390/qubs1020008>.
- [2] Otake, Compact neutron systems with fast and slow neutrons, *Plasma and Fusion Research* 13 (2018), 2401017.
- [3] Miley, Javedani, Yamamoto, Nebel, Nadler, Gu, Satsangi and Heck, Inertial-electrostatic confinement neutron/proton source, *Proceedings of 3rd International Conference on Dense Z-pinches*, AIP Press, New York (1994), pp. 675-688.
- [4] Santarius, Kulcinski, Ashley, Boris, Cipiti, Murali, Piefer, Radcliff, Radcliff and Wehmeyer, Overview of University of Wisconsin inertial-electrostatic confinement fusion research, *Fusion Science and Technology* 47 (2005), pp. 1238-1244.
- [5] Yoshikawa, Masuda, Toku, Nagasaki, Mizutani, Takamatsu, Imoto, Yamamoto, Ohnishi, Osawa, Hotta, Kohno, Okino, Watanabe, Yamauchi, Yuura, Shiroya, Tsuyoshi and Takamasa, Research and development of landmine detection system by a compact fusion neutron source, *Fusion Science and Technology* 47 (2005), pp. 1224-1228.
- [6] Yamauchi, Ohura, Watanabe, Okino, Kohno, Hotta and Yuura, Performance of neutron/proton source based on ion-source-assisted cylindrical radially convergent beam fusion, *IEEJ Transactions on Fundamentals and Materials* 126 (2006), pp. 1177-

- 1182.
- [7] Itagaki, Hotta, Hasegawa, Takakura, Tabata and Matsueda, Anode shape dependency of discharge characteristics and neutron yield of a linear type inertial electrostatic confinement fusion neutron source, *Electronics and Communications in Japan* 104 (2021), pp. 26-36.
- [8] Itagaki, Hasegawa and Hotta, Investigation of ion generation rates in an inertial electrostatic confinement device by spectroscopy-based inverse analysis, *Plasma and Fusion Research: Rapid Communications* 15 (2020), 1206070.
- [9] Tabata and Shirai, Analytic cross sections for collisions of h^+ , h_2^+ , h_3^+ , h , h_2 , and h -with hydrogen molecules, *Atomic Data and Nuclear Data Tables* 76 (2018), pp. 1-25.
- [10] Yoon, Song, Han, Hwang, Chang, Lee and Itikawa, Cross sections for electron collisions with hydrogen molecules, *Journal of Physical and Chemical Reference Data* 37 (2008), pp. 913-931.
- [11] Miley, Towner and Ivich, N. Fusion cross sections and reactivities, *Report COO-2218-17, University of Illinois, Urbana, IL, USA* (1974), <https://www.osti.gov/biblio/4014032>.
- [12] Darlington, Backscattering of 10-100 keV electrons from thick targets, *Journal of Physics D: Applied Physics* 8 (1975), pp. 85-93.
- [13] Szapiro, Rocca and Prabhuram, Electron yield of glow discharge cathode materials under helium ion bombardment, *Applied Physics Letter* 53 (1998), 358-360.
-